Rigorous Formulation of the Scattering of Plane Waves by 2-D Graphene-Based Gratings: Out-of-Plane Incidence

Ruey-Bing Hwang, *Senior Member, IEEE*

Abstract—The plane wave scattering by 2-D gratings is studied by a rigorous mode-matching technique. Specifically, the grating considered in this work is made of periodically patterned graphene. Due to the 2-D periodicity, the electromagnetic fields in the uniform medium are expressed in terms of characteristic Floquet solutions, with each space harmonic representing a plane wave solution consisting of both TE and TM constituents. By imposing the boundary condition on the tangential components of the electromagnetic fields at the graphene interface via the conductivity tensor of graphene, one can set up an input-output relation expressed in terms of the generalized scattering matrix. For a planar multilayer structure consisting of a finite stack of 2-D graphene-based gratings, the overall scattering characteristics can be obtained by cascading each of the input-output relations of the 2-D grating successively.

Index Terms—Graphene, mode-matching approach, scattering analysis, tensor conductivity, 2-D graphene-based gratings.

I. Introduction

GRAPHENE'S complex conductivity ($\sigma_g = \sigma_{g,r} + i\sigma_{g,i}$) depends on the angular frequency ω, chemical potential μ_c, temperature T, and the relaxation time of charged carriers τ. The imaginary part ($\sigma_{g,i}$), relating to the level of chemical potential, can be a positive or negative number in different ranges of operating frequencies [1], [2]. A graphene sheet with a positive value of $\sigma_{g,i}$ can support a transverse magnetic (TM) surface wave. However, when $\sigma_{g,i} < 0$, the TM surface wave no longer exists; instead, a weakly guided TE (transverse-electric) surface wave is present [3]. Plasma waves in a 2-D electron-hole system in a graphene-based heterostructure controlled by a highly conducting gate were studied [4]. The dielectric function, screening, and plasmons in 2-D graphene were investigated [5]. The method of dyadic Green's functions was developed to calculate the electromagnetic fields in the presence of an anisotropic surface conductivity model of biased graphene [6], [7].

It is interesting to note that the graphene conductivity can be dynamically altered by gate (bias) voltage in real time. Consequently, the desired conductivity patterns can be created by inhomogeneously biasing the DC voltage on a graphene layer. Several innovative applications have been proposed. For example, the SPP (surface plasma polariton) waveguide and transformation optics have been implemented using graphene by tuning its conductivity locally [3], the metamaterial-based electro-absorption THz modulators with frequency-selective-surfaces (FSS) and graphene has been developed [8], [9], and the effect of spatially dispersive phenomenon on the performance of graphene-based plasmonic devices, including phase shifters and low-pass filters, has been reported [10].

Recent studies addressed the dependence of graphene conductivity on the propagation wavenumber of the waveguide mode and concluded that the spatial dispersion becomes especially important for extremely slow waves. The spatially dispersive intraband conductivity tensor for arbitrary wave vector values was derived analytically [11]. The effect of spatial dispersion on surface waves propagation along a graphene sheet was reported [12]. The dispersion characteristics of dominant modes supported by the 2-D graphene-based waveguide were studied by using the transverse resonance technique; in particular, the spatially dispersive nature of the graphene conductivity was taken into account [13]. The propagation of surface waves along a spatially dispersive graphene-based 2-D waveguide was also investigated. Graphene was characterized by using full-k_ρ conductivity model under the relaxation-time approximation [14].

Regarding the scattering characteristics of a graphene-based periodic structure, several graphene metasurfaces were presented to show that such ultrathin surfaces could be used to dynamically control the electromagnetic wave reflection, absorption, and polarization [15]. Notably, the spatial dispersion was included in the scattering analysis; however, its influence on the scattering property was found to be negligible [16]. A reflectarray antenna based on square graphene patches was proposed to achieve good array performance, including the unit cell size reduction and grating lobe suppression [17]. The plane wave scattering and absorption by finite and infinite gratings of freestanding infinitely long graphene strips without considering the spatially dispersive nature of graphene were studied in the THz range [18].

The numerical techniques for analyzing the periodic structures made of commonly used dielectric and metallic materials

were extensively and intensively developed. For instance, the numerical methods for calculating the scattering properties of frequency selective surfaces were reviewed [19]. The rigorous coupled wave analysis (RCWA) was developed for calculating the diffraction properties of 1-D and 2-D gratings [20]. A rigorous formulation of the scattering and guiding characteristics of a 1-D dielectric grating waveguide was also reported [21]. The modal transmission line approach for analyzing the wave propagation in a multilayered structure consisting of dielectric and metallic gratings was investigated [22]. A 2-D time-domain finite-element formulation for a periodic structure was created [23]. The method of lattice sums for off-axis electromagnetic scattering by gratings was also developed [24]. Theoretical and numerical studies of plane wave scattering by gratings composed of periodic arrays of thin and lossy strips were researched [25]. Besides, the 1-D periodic surface impedance model was successfully applied to explain the Wood anomalies [26]. The 2-D periodic surface impedance model was used to evaluate the scattering characteristics [27] and the dispersion relation of waveguide modes [28] for a complex 2-D periodic structure.

In this work, we deal with the theoretical formulation of plane wave scattering by a planar multilayer structure composed of 2-D gratings made of periodically patterned graphene. Notably, the 2-D gratings considered here have the same 2-D unit cell dimensions; however, they are allowed to have different 2-D unit cell patterns. The graphene is represented by an infinitesimally thin conductive sheet, characterized by a surface conductivity obtained using a semi-classical quantum mechanical method [2]. In the mathematical formulation, we take into account the tensor conductivity of graphene, which is due mainly to magnetostatic field bias without considering spatial dispersion. As to the scalar conductivity, it can be regarded as the limiting case of a tensor conductivity by equaling the main diagonal terms and vanishing the off diagonal terms.

Concerning the theoretical formulation, we shall employ the building block approach for providing flexible computation and robust analysis. Firstly, the planar multilayer structure is decomposed into the cascade of some basic building blocks, each consisting of a 2-D periodically patterned graphene sheet sandwiched between two uniform mediums. The input-output relation of each basic building block is expressed in terms of the generalized scattering matrix. After cascading the generalized scattering matrix of each building block successively, the scattering characteristic of the whole structure can be determined accordingly. As for the mathematical procedures for determining the input-output relation is described briefly below.

The electric and magnetic fields in the uniform medium are expressed in terms of the superposition of characteristic 2-D Floquet solutions. An infinite number of space harmonics, including propagating and nonpropagating (evanescent) waves, have to be included. Each space harmonic is regarded as a plane wave consisting of hybrid modes, that is, both TE and TM polarized modes. Thus, the electric and magnetic fields in a Cartesian coordinate system to be processed will be the vector fields rather than the scalar ones. Taking into account that the surface current induced in the graphene layer is related to the tangential component of the electric field via surface conductivity, one can define the electromagnetic field boundary condition at

the graphene interface. The mode-matching technique was then used to set up an input-output relation, which is expressed in terms of the generalized scattering matrix, therein. It should be noted that a variety of numerical methods can be used to solve the problem under consideration. Some of these methods have better computational efficiency than the mode-matching approach, which needs a sufficient number of space harmonics to achieve numerical convergence. Nevertheless, the purpose of this work is to provide a physically based mathematical formulation, the transmission line network representation, to facilitate the understanding of the wave process involved in the periodic structure.

The rest of this paper is structured as follows. In Section II, we first introduce the structure configuration of the 2-D graphene-based gratings and incident condition. The mathematical formulation for setting up the electromagnetic field boundary condition via the tensor conductivity at the graphene interface is derived, together with the input-output relation of a single 2-D periodically patterned graphene; this is done in Section III. In Section IV, scattering analyses were carried out based on the mathematical formulation developed in Section III for the 1-D and 2-D periodically patterned graphene, and the multilayered structure composed of two graphene-based gratings in different layers. Additionally, the numerical simulations with CST Microwave Studio were also performed for the examples with scalar conductivity of graphene for comparison. Significantly, the scattering characteristics of 2-D periodically patterned graphene biased by magnetostatic field was also demonstrated based on our approach. The mathematical procedures for determining the eigenwave solutions in a uniform dielectric medium in the presence of 2-D periodicity are presented in Appendix A. The explicit expression for the components of the tensor conductivity of a magnetostatic and electrostatic biased graphene are listed in Appendix B.

II. DESCRIPTION OF THE PROBLEM

The problem under consideration involves 2-D graphene-based gratings embedded in a planar multilayer structure. As shown in Fig. 1, the 2-D gratings made of graphene monolayers are sandwiched between uniform dielectric layers. For a multilayer structure, the energy transmission across the layers is of primary concern, and it is natural to denote the z-axis as the longitudinal direction perpendicular to the layers.

The 2-D periodic patterns can be obtained by creating a 2-D periodic variation of the conductivity on a graphene sheet or by directly patterning a substrate. The graphene monolayer has negligible one-atom thickness. Notably, the 2-D gratings have 2-D unit cells, as shown in Fig. 2, of the same dimensions; however, they can have different unit cell patterns, the physical explanation for which will be provided later. The upper- and lower- semi-infinite half spaces are denoted as the super-strate and substrate regions, with their relative dielectric constants denoted as ε_a and ε_s, respectively. Here we consider that a plane wave is incident into the structure, with the elevation angle θ_{inc} counted from the z-axis and the azimuth angle ϕ_{inc} counted from the x-axis, as shown in Fig. 3. Such an excitation condition is called an out-of-plane incident.
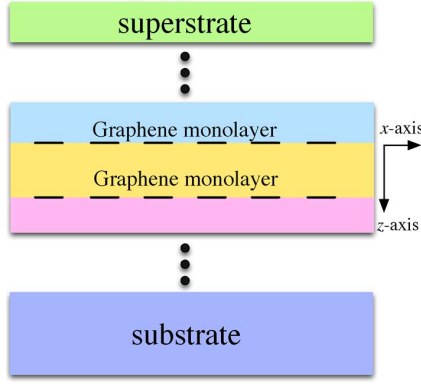
Fig. 1. Sideview of a planar multilayer structure consisting of graphene-based 2-D gratings; the layer thickness of the 2-D grating is assumed to be negligible.
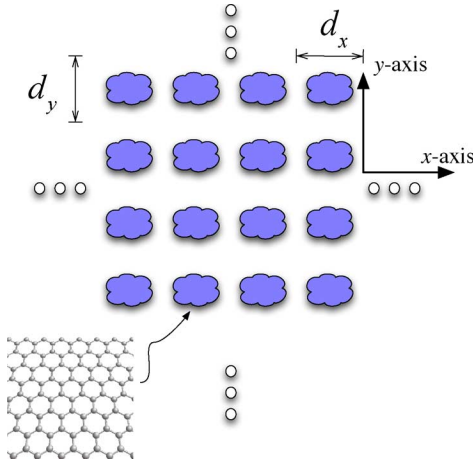

Fig. 2. 2-D graphene-based grating monolayer; the periods along the x- and y-axes are d_x and d_y, respectively. Notably, the 2-D grating can be obtained by periodically varying the graphene chemical potential or patterning the graphene directly.
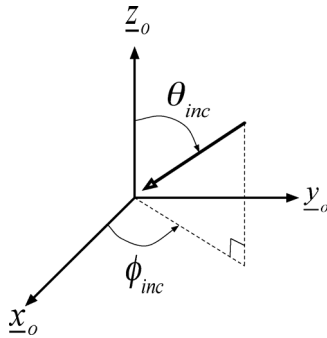

Fig. 3. Out-of-plane incident of the plane wave with angles θ_{inc} and ϕ_{inc}.

III. MATHEMATICAL FORMULATION

The mathematical procedure begins with the formulation of electric and magnetic fields in the uniform dielectric medium in the presence of 2-D periodicities along the x- and y-axes. A Floquet solution is used to express the electromagnetic field as the double Fourier series expansion with the space harmonics along the two orthogonal directions. For each space harmonic, the complete set consisting of two orthogonal eigenvectors is found to span the transverse electric and magnetic fields. The two eigenvectors correspond to the commonly used TE ($E_z = 0$)

and TM ($H_z = 0$) polarized waves. Specifically, the expansion coefficients (Floquet harmonic amplitudes) of the transverse electric (magnetic) field individually relate to the voltage (current) wave. Moreover, the voltage and current waves satisfy the 1-D transmission line equations along the z-axis.

Due to the plane wave excitation, the surface current induced in the 2-D periodically pattern graphene layer is present. The surface current density depends on the tensor conductivity of order two and the tangential component of the electric field therein. Moreover, the discontinuity of the tangential component of magnetic fields at the graphene interface is equal to the surface current density. As a consequence, one can define the boundary condition on the tangential electric and magnetic fields at the graphene interface via the tensor conductivity. In this section, the mode-matching technique will be introduced to convert the above electromagnetic boundary condition into the input-output relationship between the Floquet harmonic amplitudes in respective mediums adjacent to the single interface. Furthermore, the generalized scattering matrix (GSM) is used to represent the input-output relation and is taken as a basis for building block approach. The detailed procedure for the mathematical formulation is provided as follows.

A. Electromagnetic Fields in a Uniform Medium in the Presence of 2-D Periodicity

By the Floquet-Bloch theory, the electric and magnetic field components, with time dependence $\exp(-i\omega t)$ suppressed, can be written as

$$E_j(x,y,z) = \sum_{m=-\infty}^{\infty} \sum_{n=-\infty}^{\infty} e_{j,mn}(z)\psi_{m,n}(x,y) \quad (1)$$

$$H_j(x,y,z) = \sum_{m=-\infty}^{\infty} \sum_{n=-\infty}^{\infty} h_{j,mn}(z)\psi_{m,n}(x,y) \quad (2)$$

$$\psi_{m,n}(x,y) = \frac{\exp(ik_{x,m}x)}{\sqrt{d_x}}\frac{\exp(ik_{y,n}y)}{\sqrt{d_y}} \quad (3)$$

$$k_{x,m} = k_x + m\frac{2\pi}{d_x} \quad (4)$$

$$k_{y,n} = k_y + n\frac{2\pi}{d_y} \quad (5)$$

where $i = \sqrt{-1}$.

The function, $\psi_{m,n}(x,y)$, consisting of variables x and y is the mn^{th} Floquet harmonic that satisfies the periodic boundary conditions along the x and y axes. Additionally, the z-dependent functions corresponding to the electric and magnetic field components, $e_{j,mn}(z)$ and $h_{j,mn}(z)$, are the Fourier coefficients of the mn^{th} space harmonic. The subscript j represents x, y, or z. The periods along the x and y axes are denoted as d_x and d_y, respectively. If a plane wave is incident from the medium with relative dielectric constant denoted as ε_a, the phase constants along the x- and y-axes are written as $k_x = k_0\sqrt{\varepsilon_a}\sin\theta_{\text{inc}}\cos\phi_{\text{inc}}$ and $k_y = k_0\sqrt{\varepsilon_a}\sin\theta_{\text{inc}}\sin\phi_{\text{inc}}$, respectively.

By means of the mathematical derivation in Appendix A, for each space harmonic, the z-dependent Fourier coefficients of the electric and magnetic field components can be completely determined by solving the eigenvalue problem; the transverse components of the electric and magnetic fields can be expressed
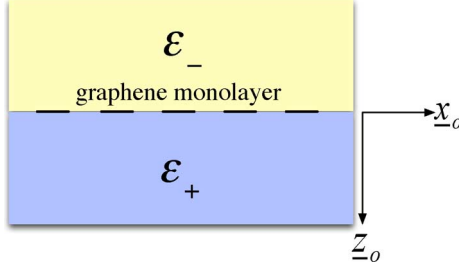
Fig. 4. Graphene-based 2-D grating located at the interface between two uniform dielectric mediums denoted as ε_+ and ε_-, respectively.

as a superposition of the orthogonally polarized fields. Consequently, the general field solutions in a uniform medium can be written as follows:

$$
\underline{z}_0 \times \underline{E}_t(x,y,z) = \sum_m \sum_n \left[v_{mn}^{(1)}(z)\underline{\alpha}_{mn}^{(1)} + v_{mn}^{(2)}(z)\underline{\alpha}_{mn}^{(2)} \right]
$$
$$
\cdot \psi_{mn}(x,y) \tag{6}
$$
$$
\underline{H}_t(x,y,z) = \sum_m \sum_n \left[i_{mn}^{(1)}(z)\underline{\alpha}_{mn}^{(1)} + i_{mn}^{(2)}(z)\underline{\alpha}_{mn}^{(2)} \right]
$$
$$
\cdot \psi_{mn}(x,y). \tag{7}
$$

Parameters $v_{mn}^{(l)}(z)$ and $i_{mn}^{(l)}(z)$ are the transmission line voltage and current along the z-axis given in (A13) and (A14), where $l = 1$ stands for TE polarization and $l = 2$ for TM polarization, respectively; $\underline{\alpha}_{mn}^{(1)}$ and $\underline{\alpha}_{mn}^{(2)}$ are two orthogonal eigenvectors given in Appendix A.

The above equations reveal that each space harmonic appears as a plane wave with the transverse field components generally represented as a superposition of the TE- and TM-polarized plane waves.

B. Conduction Current on the Graphene Monolayer

As shown in Fig. 4, the graphene grating locates on the $z = 0$ plane; the graphene layer is sandwiched between two uniform dielectric mediums, with the relative dielectric constants denoted as ε_+ and ε_-, respectively. From the electromagnetic boundary condition, the discontinuity of the magnetic fields on the two opposite sides at the interface, $z = 0$, is due to the conduction current induced in the graphene monolayer, which is written as

$$
\underline{z}_0 \times \left[\underline{H}(\rho, 0^+) - \underline{H}(\rho, 0^-) \right] = \underline{J}_c(\rho, 0) \tag{8}
$$

where $\rho = x\underline{x}_0 + y\underline{y}_0$. The notations 0^+ and 0^- are designated as the positions of $z = 0 + \epsilon$ and $z = 0 - \epsilon$, respectively, with $\epsilon \to 0$.

The conduction current is relevant to the transverse electric field on the graphene sheet via a tensor conductivity of graphene $\underline{\underline{\sigma}}_t$, which is written as

$$
\underline{J}_c(\rho, 0) = \underline{\underline{\sigma}}_t(x,y,\omega) \cdot \underline{E}_t(\rho, 0) \tag{9}
$$

with

$$
\underline{\underline{\sigma}}_t(x,y,\omega) = \sigma_{xx}(x,y,\omega)\underline{x}_0\underline{x}_0 + \sigma_{xy}(x,y,\omega)\underline{x}_0\underline{y}_0
$$
$$
+ \sigma_{yx}(x,y,\omega)\underline{y}_0\underline{x}_0 + \sigma_{yy}(x,y,\omega)\underline{y}_0\underline{y}_0. \tag{10}
$$

The x and y components in (8) are written below, respectively

$$
H_x(\rho, 0^+) - H_x(\rho, 0^-)
$$
$$
= \sigma_{yx}(x,y,\omega)E_x(\rho,0) + \sigma_{yy}(x,y,\omega)E_y(\rho,0) \tag{11}
$$
$$
H_y(\rho, 0^+) - H_y(\rho, 0^-)
$$
$$
= -\sigma_{xx}(x,y,\omega)E_x(\rho,0) - \sigma_{xy}(x,y,\omega)E_y(\rho,0). \tag{12}
$$

Substitution of (6) and (7) into (11) and (12), we obtain the two equations given below

$$
\sum_m \sum_n \left[h_{x,mn}(0^+) - h_{x,mn}(0^-) \right] \psi_{mn}(x,y)
$$
$$
= \sum_m \sum_n \left[\sigma_{yx}(x,y,\omega)e_{x,mn}(0) + \sigma_{yy}(x,y,\omega)e_{y,mn}(0) \right]
$$
$$
\cdot \psi_{mn}(x,y) \tag{13}
$$
$$
\sum_m \sum_n \left[h_{y,mn}(0^+) - h_{y,mn}(0^-) \right] \psi_{mn}(x,y)
$$
$$
= -\sum_m \sum_n \left[\sigma_{xx}(x,y,\omega)e_{x,mn}(0) + \sigma_{xy}(x,y,\omega)e_{y,mn}(0) \right]
$$
$$
\cdot \psi_{mn}(x,y). \tag{14}
$$

For the sake of succinctness, we group the index pair (m,n) and denote it as a new integer p; that is, $p \to (m,n)$, where p ranges from 1 to ∞. The new index p represents the pth space harmonics pair, which is arranged in ascending order of the cutoff frequencies of the space harmonics. Therefore, (13) can be rewritten as

$$
\sum_{p=1}^{\infty} \left[h_{x,p}(0^+) - h_{x,p}(0^-) \right] \psi_p(x,y)
$$
$$
= \sum_{p=1}^{\infty} \left[\sigma_{yx}(x,y,\omega)e_{x,p}(0) + \sigma_{yy}(x,y,\omega)e_{y,p}(0) \right] \psi_p(x,y). \tag{15}
$$

Multiplying (15) with $\psi_q^\dagger(x,y)$ at both sides and taking the integral over the unit cell of the 2-D periodic structure, we obtain the equation given below

$$
h_{x,q}(0^+) - h_{x,q}(0^-) = \sum_{p=1}^{\infty} c_{yx}^{q,p} e_{x,p}(0) + c_{yy}^{q,p} e_{y,p}(0) \tag{16}
$$

with

$$
c_{yx}^{q,p} = \int_{d_x} \int_{d_y} \psi_q^\dagger(x,y)\sigma_{yx}(x,y,\omega)\psi_p(x,y)dxdy \tag{17}
$$
$$
c_{yy}^{q,p} = \int_{d_x} \int_{d_y} \psi_q^\dagger(x,y)\sigma_{yy}(x,y,\omega)\psi_p(x,y)dxdy \tag{18}
$$
$$
\delta_{pq} = \int_{d_x} \int_{d_y} \psi_q^\dagger(x,y)\psi_p(x,y)dxdy \tag{19}
$$

where the symbol "$\dagger$" represents the complex conjugate and δ_{pq} is the Kronecker delta.

Notably, the index q stands for the index pair of (r,s). Equation (16) forms a system of linear equations with q running from 1 to infinity. It can be expressed in terms of the matrix form given below

$$
\underline{h}_x(0^+) - \underline{h}_x(0^-) = \boldsymbol{C}_{yx}\underline{e}_x(0) + \boldsymbol{C}_{yy}\underline{e}_y(0). \tag{20}
$$

Repeat the aforementioned procedure for (14), we obtain the matrix equation given below

$$\underline{h}_y(0^+) - \underline{h}_y(0^-) = -\boldsymbol{C}_{xx}\underline{e}_x(0) - \boldsymbol{C}_{xy}\underline{e}_y(0) \quad (21)$$

where $\boldsymbol{C}_{xx}$ and $\boldsymbol{C}_{xy}$ are full matrices with the $(q,p)^{th}$ entry written below

$$c_{xx}^{q,p} = \int_{d_x}\int_{d_y} \psi_q^\dagger(x,y)\sigma_{xx}(x,y,\omega)\psi_p(x,y)dxdy \quad (22)$$

$$c_{xy}^{q,p} = \int_{d_x}\int_{d_y} \psi_q^\dagger(x,y)\sigma_{xy}(x,y,\omega)\psi_p(x,y)dxdy. \quad (23)$$

If the spatially dispersive nature is considered (under the condition of vanishing electrostatic and magnetostatic bias, at room temperature), the conductivity tensor $\hat{\underline{\underline{\sigma}}}$ in (10) will become a differential operator [7] with the diagonal terms $\hat{\sigma}_{xx} = \sigma_{lo} + \alpha_{sd}\partial^2/\partial x^2 + \beta_{sd}\partial^2/\partial y^2$ and $\hat{\sigma}_{yy} = \sigma_{lo} + \beta_{sd}\partial^2/\partial x^2 + \alpha_{sd}\partial^2/\partial y^2$ and with the off-diagonal terms $\hat{\sigma}_{xy} = \hat{\sigma}_{yx} = 2\beta_{sd}\partial^2/\partial x\partial y$. The parameters σ_{lo}, α_{sd} and β_{sd} can be found in [7], [12]. Notably, the aforementioned conductivity model in [7] is based on low-k_ρ approximations, i.e., only valid when the wavenumber is sufficiently fast and up to THz frequencies. Otherwise, the spatially-dispersive conductivity model defined in [11] should be employed, which is much more complex and clearly out of the scope of this paper.

Equations (17), (18), (22), and (23) can then be modified as given below

$$c_{xx}^{q,p} = \int_{d_x}\int_{d_y} \psi_q^\dagger(x,y)(\sigma_{lo}-\alpha_{sd}k_{xm}^2-\beta_{sd}k_{yn}^2)\psi_p(x,y)dxdy \quad (24)$$

$$c_{xy}^{q,p} = \int_{d_x}\int_{d_y} \psi_q^\dagger(x,y)(-2\beta_{sd}k_{xm}k_{yn})\psi_p(x,y)dxdy \quad (25)$$

$$c_{yy}^{q,p} = \int_{d_x}\int_{d_y} \psi_q^\dagger(x,y)(\sigma_{lo}-\beta_{sd}k_{xm}^2-\alpha_{sd}k_{yn}^2)\psi_p(x,y)dxdy \quad (26)$$

with $c_{yx}^{q,p} = c_{xy}^{q,p}$ and $p \to (m,n)$.

We may again set up a matrix equation by reorganizing (20) and (21), given below

$$\begin{bmatrix} \underline{h}_x(0^+) \\ \underline{h}_y(0^+) \end{bmatrix} - \begin{bmatrix} \underline{h}_x(0^-) \\ \underline{h}_y(0^-) \end{bmatrix} = \tilde{\boldsymbol{C}} \begin{bmatrix} -\underline{e}_y(0) \\ \underline{e}_x(0) \end{bmatrix} \quad (27)$$

$$\tilde{\boldsymbol{C}} = \begin{bmatrix} -\boldsymbol{C}_{yy} & \boldsymbol{C}_{yx} \\ \boldsymbol{C}_{xy} & -\boldsymbol{C}_{xx} \end{bmatrix}. \quad (28)$$

From (A11), the x and y components of the electric field can be written explicitly as

$$e_{x,mn}(z) = v_{mn}^{(1)}(z)\frac{k_{yn}}{k_{tmn}} + v_{mn}^{(2)}(z)\frac{k_{xm}}{k_{tmn}} \quad (29)$$

$$-e_{y,mn}(z) = v_{mn}^{(1)}(z)\frac{k_{xm}}{k_{tmn}} - v_{mn}^{(2)}(z)\frac{k_{yn}}{k_{tmn}}. \quad (30)$$

We collect each space harmonic of the transverse electric field component and put them into a super-vector. The matrix equation is written below

$$\begin{bmatrix} -\underline{e}_y(z) \\ \underline{e}_x(z) \end{bmatrix} = \tilde{\boldsymbol{A}} \begin{bmatrix} \underline{v}^{(1)}(z) \\ \underline{v}^{(2)}(z) \end{bmatrix} \quad (31)$$

$$\tilde{\boldsymbol{A}} = \begin{bmatrix} \boldsymbol{A}_x & -\boldsymbol{A}_y \\ \boldsymbol{A}_y & \boldsymbol{A}_x \end{bmatrix}. \quad (32)$$

Parameter $\underline{e}_j(z)$ is a column vector with each element equal to $e_{j,mn}$, where the subscript j represents x or y. Parameters $\boldsymbol{A}_x$ and $\boldsymbol{A}_y$ are diagonal matrices with k_{xm}/k_{tmn} and k_{yn}/k_{tmn} filled at their diagonal entry, respectively. Column vector $\underline{v}^{(k)}(z)$ has the element $v_{mn}^{(k)}(z)$, where $k = 1$ for TE polarization, and 2 for TM polarization. Similarly, the transverse components of the magnetic field can also be expressed in terms of the form similar to (31), given as follows:

$$\begin{bmatrix} \underline{h}_x(z) \\ \underline{h}_y(z) \end{bmatrix} = \tilde{\boldsymbol{A}} \begin{bmatrix} \underline{i}^{(1)}(z) \\ \underline{i}^{(2)}(z) \end{bmatrix}. \quad (33)$$

The definition of $\underline{h}_x(z)$, $\underline{h}_y(z)$, $\underline{i}^{(1)}(z)$, and $\underline{i}^{(2)}(z)$ remains the same as described previously.

The voltage and current vectors in the right-hand side of (31) and (33), in fact, can be written in terms of the transmission-line solution given below

$$\underline{v}(z) = \begin{bmatrix} \underline{v}^{(1)}(z) \\ \underline{v}^{(2)}(z) \end{bmatrix}$$
$$= diag\left(\exp[i\underline{k}_z z]\right)\underline{a} + diag\left(\exp[-i\underline{k}_z z]\right)\underline{b} \quad (34)$$

$$\underline{i}(z) = \begin{bmatrix} \underline{i}^{(1)}(z) \\ \underline{i}^{(2)}(z) \end{bmatrix}$$
$$= \tilde{\boldsymbol{Y}}_c \left\{ diag\left(\exp[i\underline{k}_z z]\right)\underline{a} - diag\left(\exp[-i\underline{k}_z z]\right)\underline{b} \right\}. \quad (35)$$

Where the notation $diag(\dots)$ represents the diagonal matrix with the diagonal entries equal to the vector inside the round brackets. Parameter $\tilde{\boldsymbol{Y}}_c$ is a diagonal matrix with its entry representing TE and TM wave admittances given in (A15) and (A16), respectively.

Parameter $\underline{k}_z$ is a column vector with each entry representing the z-direction propagation constant of each space harmonic, as

$$\underline{k}_z = \begin{bmatrix} \underline{k}_z^{(1)} \\ \underline{k}_z^{(2)} \end{bmatrix}. \quad (36)$$

Notice that $\underline{k}_z^{(1)}$ and $\underline{k}_z^{(2)}$ are equal to each other in the uniform medium. The vectors $\underline{a}$ and $\underline{b}$ are respectively taken as the forward- and backward- propagation waves along the transmission line, each of which contains the TE- and TM-polarized space harmonic amplitudes, as given below

$$\underline{a} = \begin{bmatrix} \underline{a}^{(1)} \\ \underline{a}^{(2)} \end{bmatrix} \quad (37)$$

$$\underline{b} = \begin{bmatrix} \underline{b}^{(1)} \\ \underline{b}^{(2)} \end{bmatrix}. \quad (38)$$

Substitution of (31) and (33) into (27), we obtain:

$$\tilde{\boldsymbol{A}}\underline{i}(0^+) - \tilde{\boldsymbol{A}}\underline{i}(0^-) = \tilde{\boldsymbol{C}}\tilde{\boldsymbol{A}}\underline{v}(0). \quad (39)$$

From the electromagnetic boundary condition, the tangential electric fields must be continuous at the interface (the graphene grating sheet) between the two uniform dielectric mediums. Therefore, we may have the equation given below

$$\tilde{\boldsymbol{A}}\underline{v}(0^+) = \tilde{\boldsymbol{A}}\underline{v}(0^-). \quad (40)$$

Notably, the matrix $\tilde{A}$ remains the same for the two regions above and beneath the graphene sheet due to the phase match condition, i.e., the transverse propagation vector, $\underline{k}_{t,mn}$, must be continuous at the interface between the two adjacent dielectric mediums.

C. Input-Output Relation of the 2-D Graphene-Based Grating Monolayer: Generalized Scattering Matrix Method

By the electromagnetic boundary conditions at the graphene monolayer, we obtain the relationship for the voltage and current vectors therein, which are (39) and (40). With the voltage and current vectors containing the incident and reflected vectors at the interface in respective regions, we may determine the input-output relation at the graphene interface in terms of the commonly used generalized scattering matrix representation [29]. Substitution of (34) and (35) into (39) and (40) and via a intuitive derivation, we may obtain the generalized scattering matrix defined at the graphene interface, which is given below

$$\begin{bmatrix} \underline{b}_1 \\ \underline{b}_2 \end{bmatrix} = \tilde{S}_g \begin{bmatrix} \underline{a}_1 \\ \underline{a}_2 \end{bmatrix} \tag{41}$$

where

$$\tilde{S}_g = \begin{bmatrix} I & -I \\ \tilde{Y}_c^{(-)} - \tilde{A}^T \tilde{C} \tilde{A} & \tilde{Y}_c^{(+)} \end{bmatrix}^{-1}$$
$$\cdot \begin{bmatrix} -I & I \\ \tilde{Y}_c^{(-)} + \tilde{A}^T \tilde{C} \tilde{A} & \tilde{Y}_c^{(+)} \end{bmatrix} \tag{42}$$

where I is the identity matrix.

Moreover, for a general structure shown in Fig. 1, we may first partition it into several constituent parts, each composed of a single 2-D graphene-based grating layer. The scattering matrix corresponding to each graphene grating can be independently determined via (42). By cascading all the generalized scattering matrices, we obtain a global generalized scattering matrix and determine the scattering characteristic of the overall structure. The detail mathematical procedures can be found in [29], [31].

I emphasize once again that all the 2-D gratings have the same unit cell size but may have different unit cell patterns. For the multiple gratings with different periods, the multiple periods along the same direction result in more and more space harmonics [30]. For example, let us consider two periods a and b along the x-axis. The mth space harmonic (with phase constant $k_x + m2\pi/a$) due to the grating "a" is incident into the grating "b," enabling the new phase constant: $(k_x + m2\pi/a) + n2\pi/b$, where the index n belongs to the grating "b." This problem is more complicated and beyond the scope of this research. The present paper focuses on 2-D gratings with the same unit cell dimensions.

IV. NUMERICAL RESULTS

With the rigorous formulation outlined in Section III, the plane-wave scattering characteristics of graphene-based 2-D gratings can be systematically investigated. We have considerably carried out numerical simulations to establish the validity and accuracy of the analysis method employed. However, four numerical examples were presented due to space limitations. In the first three examples, the graphene conductivity is a scalar
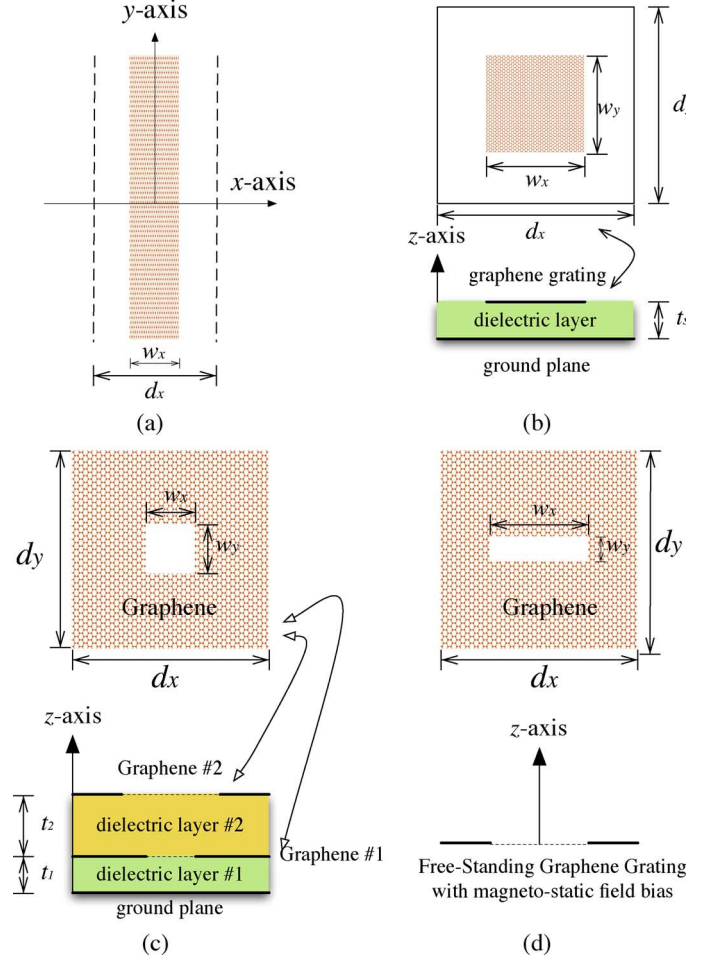

Fig. 5. Structure configuration (side view) and unit cell pattern of the periodically patterned graphene employed in the numerical calculation: (a) the free-standing 1-D array of graphene strips, (b) the 2-D square graphene patches array coated on a grounded dielectric slab, (c) the planar multilayer structure consisting of two layers of periodically patterned graphene, and (d) the 2-D array of rectangular apertures perforated on a freestanding graphene layer. The ground plane shown in (b) and (c) is made of perfect electric conductor.

(electrostatic bias, no magnetostatic bias nor spatial dispersion) with the conductivity $\sigma_d(\mu_c(E_o))$. The fourth example is for the case of a tensor conductivity with both magnetostatic- and electrostatic-bias (without spatial dispersion). The tensor conductivity can be written as $\sigma_{xx} = \sigma_{yy} = \sigma_d(\mu_c(E_o), B_o)$ and $\sigma_{xy} = -\sigma_{yx} = \sigma_o(\mu_c(E_o), B_o)$, with the formulas given in Appendix B [7].

In the first example, the plane wave absorbance by the 1-D graphene-strip grating shown in [18, Fig. 11] was taken as a benchmark for checking the accuracy of our computer code. Referring to Fig. 5(a), a plane wave is normally incident on a freestanding 1-D strip grating made of graphene. The period and strip width along the x-axis are 70 μm and 20 μm, respectively. The graphene parameters are $\mu_c = 0.39$ eV and $\tau = 1$ ps at room temperature $T = 300°$K. For the 1-D periodic structure, our 2-D code can still work well when a very small period is set along the y-axis ($w_y = d_y = 0.01$ μm, for example). Fig. 6 shows the numerical results on the absorption efficiency for both TE- and TM-incident plane waves. The solid line indicates the
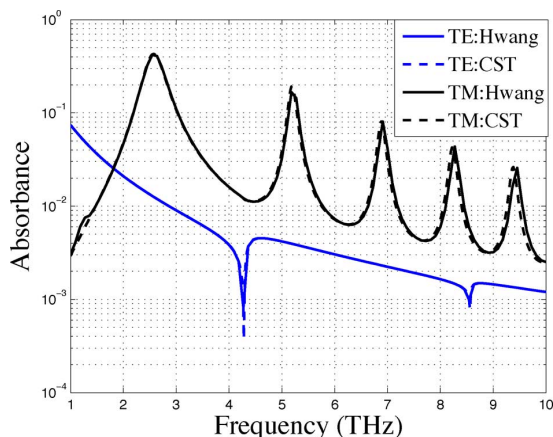
Fig. 6. Plane wave absorption versus frequency for a 1-D graphene grating shown in Fig. 5(a). The graphene parameters are $\mu_c = 0.39$ eV and $\tau = 1$ ps at room temperature $T = 300°$K. The period and strip width along the x-axis are $d_x = 70$ μm and $w_x = 20$ μm, respectively.
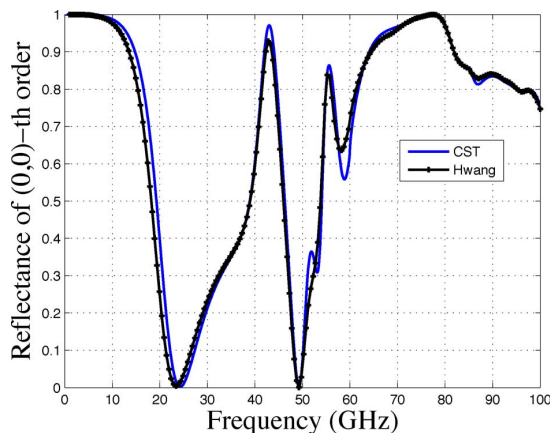

Fig. 7. Reflectance of the fundamental space harmonic against frequency for a 2-D graphene grating deposited on a grounded dielectric slab shown in Fig. 5(b), under the normal incidence of a plane wave (E_x-polarized). The graphene parameters are given below: $\mu_c = 0.3$ eV and $\tau = 1$ ps at room temperature $T = 300°$K. The periods of the unit cell are $d_x = 5$ mm and $d_y = 5$ mm; the unit-cell pattern is a square graphene patch with the widths $w_x = 2.5$ mm and $w_y = 2.5$ mm. The relative dielectric constant and thickness of the dielectric slab are $\varepsilon_s = 3.75$ and $t_s = 1$ mm.
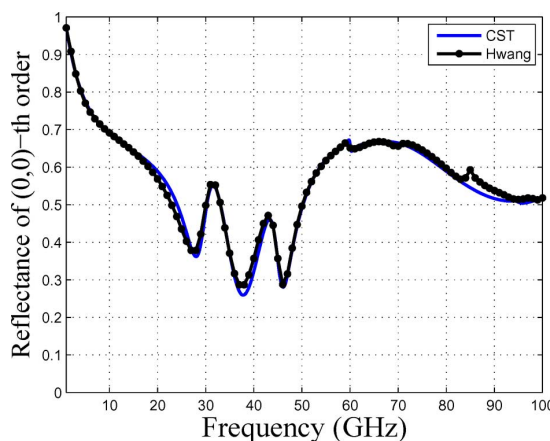
curves calculated based on the code developed in this paper, whereas the dashed line denotes the curves obtained by using the commercial software CST Microwave Studio. In the numerical simulation with CST, the surface impedance $Z_s (= 1/\sigma_d)$ was used to model the graphene sheet with zero thickness. Apparently, we obtained excellent agreement between the two results for both TE and TM polarization. Notably, the results also coincide with those shown in [18, Fig. 11].

In the second example, we calculate the reflectance of a 2-D periodically patterned graphene coated onto a grounded dielectric slab, with the unit cell pattern depicted in Fig. 5(b). The unit cell pattern is a square lattice with lattice constant 5 mm; the width of the square graphene patch is 2.5 mm. The relative dielectric constant and thickness of the dielectric slab are $\varepsilon_s = 3.75$ and $t_s = 1$ mm. The graphene parameters are $\mu_c = 0.3$ eV and $\tau = 1$ ps at room temperature $T = 300°$K. The plane wave is normally incident on the 2-D periodic structure with E_x-polarized. The reflectance of the fundamental space harmonic, $(0,0)^{th}$ order, are calculated. Referring to Fig. 7, the curve in solid line and plus markers is obtained using our approach, whereas the curve in blue line is via the CST simulation. Apparently, they generally agree except for a slight discrepancy.

Additionally, the planar multilayer structure consisting of two graphene-based gratings and two uniform dielectric layers was considered for calculating the plane-wave scattering properties. The structure configuration is shown in Fig. 5(c). Since the structure is terminated by a metal ground plane (PEC), only the reflection waves are observed. The chemical potential (μ_c) for the upper and lower graphene sheets are 0.3 eV and 0.1 eV, respectively; however, they share the same relaxation time $\tau = 1$ ps at room temperature $T = 300°$K. Both gratings have the same unit cell dimension (square lattice with lattice constant 5 mm). The unit cell pattern is also shown in Fig. 5(c). The dimension of the square apertures are 2.5 mm for the upper graphene layer and 1 mm for the lower graphene layer, respectively; the thickness and relative dielectric constant of the two dielectric layers are: $\varepsilon_1 = 3.75$, $t_1 = 0.5$ mm (lower layer), and $\varepsilon_2 = 3.9$, $t_2 = 1.0$ mm (upper layer). As shown in Fig. 8, the curve with circle markers is obtained using the approach

Fig. 8. Reflectance of the fundamental space harmonic, $(0,0)^{th}$-order, against the frequency for the multilayered structure depicted in Fig. 5(c), under the normal incidence of E_x-polarized plane wave. The graphene parameters for the upper layer are $\mu_c = 0.3$ eV and $\tau = 1$ ps; the lower one has the parameters: $\mu_c = 0.1$ eV and $\tau = 1$ ps, both are at room temperature $T = 300°$K. The dimension of the square lattice is 5 mm for both gratings; the unit-cell pattern of the graphene grating is also shown in Fig. 5(c). The dimension of the apertures are 2.5 mm × 2.5 mm for the upper layer and 1 mm × 1 mm for the lower layer, respectively; the relative dielectric constant and thickness of the two dielectric layers are: $\varepsilon_1 = 3.75, t_1 = 0.5$ mm (lower layer), and $\varepsilon_2 = 3.9, t_2 = 1.0$ mm (upper layer).

presented in this paper, whereas that in solid and blue line is via CST simulation. The excellent agreement between the two results prove that our approach indeed can handle the scattering analysis of a structure composed of multiple graphene gratings.

Fig. 9 depicts the scattering characteristics, including the reflectance and transmittance, of a magnetostatically and electrostatically biased graphene, under normal incidence of plane wave. Referring to Fig. 5(d), a freestanding graphene layer is etched periodically to create a lattice of slots. Each slot has the dimensions $w_x = 5$ mm and $w_y = 1$ mm. The periods along both the x- and y-axes are $d_x = d_y = 10$ mm. The graphene parameter is $\tau = 3$ ps at room temperature
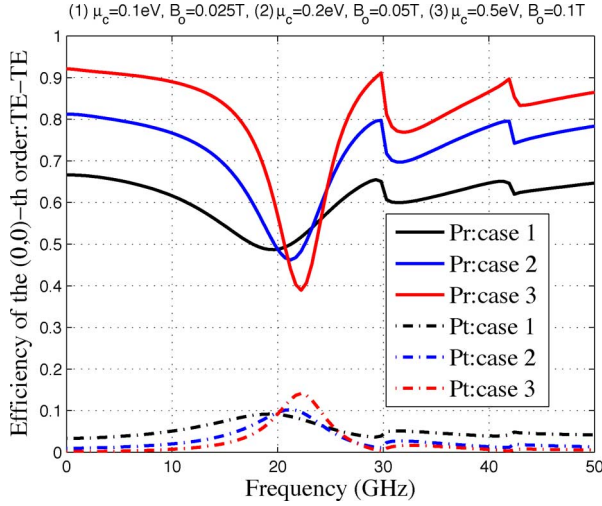
Fig. 9. Scattering efficiency versus frequency for a freestanding 2-D graphene grating, as shown in Fig. 5(d), under the normal incidence of a plane wave. The chemical potential and biased magnetostatic field strength for the three cases are given as follows: (1) $\mu_c = 0.1$ eV $B_o = 0.025$ T, (2) $\mu_c = 0.2$ eV $B_o = 0.05$ T, and (3) $\mu_c = 0.5$ eV $B_o = 0.1$ T. The relaxation time for the three case all are $\tau = 3$ ps at room temperature $T = 300°$K. The periods along the x- and y-axes are $d_x = 10$ mm, $d_y = 10$ mm, the slot widths along the x- and y-axes $w_x = 5$ mm and $w_y = 1$ mm. In the legend, "Pr" and "Pt" represent the reflected and transmitted power, respectively; they are normalized to the incident power.
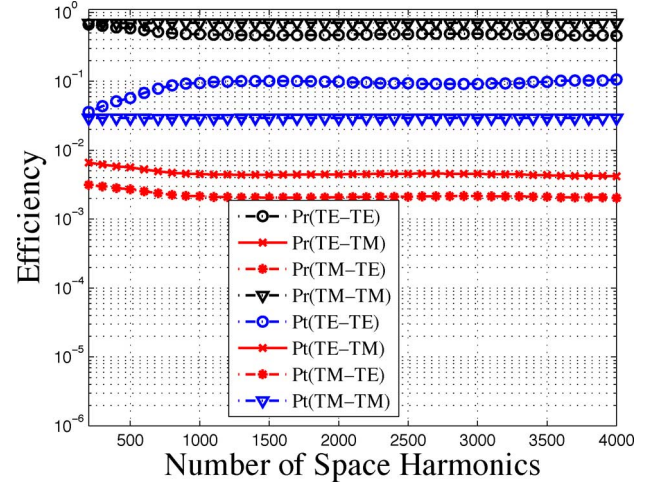

Fig. 10. Scattering efficiency versus truncated number of space harmonics employed for numerical calculation for the first case in the previous example (operation frequency is 20 GHz). The chemical potential and biased magnetostatic field strength are $\mu_c = 0.1$ eV $B_o = 0.025$ T. The graphene parameter is $\tau = 3$ ps at room temperature $T = 300°$K. The periods along the x- and y-axes are $d_x = 10$ mm and $d_y = 10$ mm; the slot dimensions along the x- and y-axes are $w_x = 5$ mm and $w_y = 1$ mm. In the legend, 'Pr' and 'Pt' mean the reflected and transmitted power, respectively, which are normalized to the incident power. The polarization of the input and output wave are indicated in the format of Pr (input-output); for example, Pt (TM-TE) calculates the cross-polarization efficiency of the incident TM-polarized plane wave.

$T = 300°$K. The three different applied bias electrostatic and magnetostatic fields are given as follows: (1) $\mu_c = 0.1$ eV and $B_o = 0.025$ T, (2) $\mu_c = 0.2$ eV and $B_o = 0.05$ T, and (3) $\mu_c = 0.5$ eV and $B_o = 0.1$ T. The tensor conductivity of graphene corresponding to each condition can be obtained through (B.1) and (B.2) in Appendix B. The electric field vector is along the y-axis for the TE incident plane wave and along the x-axis for TM wave. Here, we demonstrate the reflectance and transmittance of the dominant space harmonic, $(0, 0)^{th}$ order. Apparently, the scattering property was altered by changing the electrostatic and magnetostatic bias. Compared with a PEC sheet equipped with the same slots array, the phenomenon of extraordinary transmission through a sub-wavelength holes array was observed (the resonance transmission peak for the PEC slotted array counterpart occurs at 25.35 GHz). This is due to the well-known slow-wave propagation associated with graphene plasmonic modes. Moreover, drastic changes in the reflectance occur at 29.979 GHz and 42.397 GHz; they are due to the onset of the first higher-order $((0, \pm 1)$ or $(\pm 1, 0))$ and second higher-order $((1, \pm 1)$ or $(-1, \pm 1))$ space harmonics, respectively. Because they are related to the periodicity rather than to the graphene parameters, the cutoff frequencies of the three cases are consistent.

Notably, the numerical convergence in the scattering analysis against the truncated number of space harmonics has been investigated thoroughly in the previous examples. Due to space limitations, only the convergence test for the first case around the transmission peak (20 GHz) in Fig. 9 is shown. In Fig. 10, the vertical axis represents the scattering efficiency of the TE- or TM- polarized plane wave under normal incidence, whereas the horizontal axis represents the number of truncated space

harmonics. The cross-polarization coupling observed in this figure is due to the off-diagonal entries of the tensor conductivity ($\sigma_{xy} = -\sigma_{yx} = +\sigma_o$) caused by the magnetostatic field bias. For instance, the incident E_y-polarized electric field induces the E_x-polarized electric field (TM-polarized wave) through σ_{xy}. Returning to Fig. 10, apparently, the reflectance and transmittance converge (the variance is within 0.1%) as the number of space harmonics is greater than 3000 (1500 TE and 1500 TM space harmonics, respectively).

V. CONCLUSION

In summary, we have presented a rigorous formulation for dealing with the plane wave scattering by 2-D graphene-based gratings. The boundary conditions on the electromagnetic fields at the interface of a periodically patterned graphene layer is set up via the conductivity tensor of graphene. The mode-matching technique is then employed for determining the input-output relation therein. Significantly, for a planar multilayer structure comprised of a finite stack of 2-D graphene-based grating layers, each of which can be analyzed independently for determining their generalized scattering matrices. After successively cascading the generalized scattering matrices, the scattering properties of the overall structure can be determined accordingly. A good agreement was obtained between the results of this approach and those of the CST Microwave Studio in terms of the scattering analyses of the prescribed 1-D and 2-D graphene gratings with scalar conductivity. Moreover, a scattering analysis of the graphene grating with tensor conductivity due to magnetostatic field bias was also carried out.

APPENDIX A
EIGEN-WAVE IN A UNIFORM DIELECTRIC MEDIUM IN THE PRESENCE OF 2-D PERIODICITY

We first substitute electric- and magnetic- field components in (1) and (2) into Faraday's law of induction, with the curl operator and field vector decomposed into the transverse and longitudinal components, such as $\nabla = \nabla_t + \underline{z}_0 \partial/\partial z$ and $\underline{F} = \underline{F}_t + \underline{z}_0 F_z$, where $\nabla_t = \underline{x}_0 \partial/\partial x + \underline{y}_0 \partial/\partial y$ and $\underline{F} = \underline{E}$ or $\underline{H}$. We obtained the two equations given below

$$\underline{k}_{t,mn} \times \underline{e}_{t,mn}(z) = \omega\mu_0 \underline{h}_{z,mn}(z) \tag{A1}$$

and

$$i\underline{k}_{t,mn} \times \underline{e}_{z,mn}(z) + \frac{d}{dz}\underline{z}_0 \times \underline{e}_{t,mn} = i\omega\mu_0 \underline{h}_{t,mn}(z). \tag{A2}$$

Substituting electric- and magnetic- field components in (1) and (2) into the Ampere's law with Maxwell modification, we obtain the following two equations corresponding to the transverse and longitudinal components of the vector fields, respectively

$$-\underline{k}_{t,mn} \times \underline{h}_{t,mn}(z) = \omega\varepsilon_0\varepsilon_s \underline{e}_{z,mn}(z) \tag{A3}$$

and

$$i\underline{k}_{t,mn} \times \underline{h}_{z,mn}(z) + \frac{d}{dz}\underline{z}_0 \times \underline{h}_{t,mn} = -i\omega\varepsilon_0\varepsilon_s \underline{e}_{t,mn}(z). \tag{A4}$$

Substituting (A3) into (A2) and eliminating $\underline{e}_{z,mn}$, we obtain the differential equation give below

$$\frac{d}{dz}\left(\underline{z}_0 \times \underline{e}_{t,mn}\right) = \underline{\underline{\zeta}} \cdot \underline{h}_{t,mn} \tag{A5}$$

$$\underline{\underline{\zeta}} = i\frac{k_z^2 \underline{\underline{I}} + \underline{k}_{t,mn}\underline{k}_{t,mn}}{\omega\varepsilon_0\varepsilon_s} \tag{A6}$$

where $\underline{\underline{I}}$ is the 2-D unit dyadic and $\underline{\underline{\zeta}}$ is a 2-D dyadic. The phase relation of the Floquet modes (plane-wave solutions) satisfies $k_z^2 + k_{t,mn}^2 = k_0^2\varepsilon_s$, where $\underline{k}_{t,mn} = k_{xm}\underline{x}_0 + k_{yn}\underline{y}_0$.

Substitution of (A1) into (A4) by eliminating $\underline{h}_{z,mn}$, the other differential equation can be determined as follows:

$$\frac{d}{dz}\underline{h}_{t,mn} = \underline{\underline{\eta}} \cdot \left(\underline{z}_0 \times \underline{e}_{t,mn}\right) \tag{A7}$$

$$\underline{\underline{\eta}} = i\frac{k_o^2\varepsilon_s \underline{\underline{I}} - \underline{k}_{t,mn}\underline{k}_{t,mn}}{\omega\mu_0} \tag{A8}$$

where $\underline{\underline{\eta}}$ is a 2-D dyadic.

By solving the eigenvalues ($\lambda_{mn}^{(1)}$ and $\lambda_{mn}^{(2)}$) and associated eigenvectors ($\underline{\alpha}_{mn}^{(1)}$ and $\underline{\alpha}_{mn}^{(2)}$), the 2-D dyadic $\underline{\underline{\zeta}}$ can be spanned using the previous two eigenvectors written as

$$\underline{\underline{\zeta}} = \lambda_{mn}^{(1)}\underline{\alpha}_{mn}^{(1)}\underline{\alpha}_{mn}^{(1)} + \lambda_{mn}^{(2)}\underline{\alpha}_{mn}^{(2)}\underline{\alpha}_{mn}^{(2)}. \tag{A9}$$

Similarly, the 2-D dyadic $\underline{\underline{\eta}}$ is expanded using the two eigenvectors written as

$$\underline{\underline{\eta}} = \rho_{mn}^{(1)}\underline{\alpha}_{mn}^{(1)}\underline{\alpha}_{mn}^{(1)} + \rho_{mn}^{(2)}\underline{\alpha}_{mn}^{(2)}\underline{\alpha}_{mn}^{(2)}. \tag{A10}$$

The transverse components of the electric- and magnetic-field vector can then be spanned using the two prescribed eigenvectors, which are written as

$$\underline{z}_0 \times \underline{e}_{t,mn}(z) = v_{mn}^{(1)}(z)\underline{\alpha}_{mn}^{(1)} + v_{mn}^{(2)}(z)\underline{\alpha}_{mn}^{(2)} \tag{A11}$$

$$\underline{h}_{t,mn}(z) = i_{mn}^{(1)}(z)\underline{\alpha}_{mn}^{(1)} + i_{mn}^{(2)}(z)\underline{\alpha}_{mn}^{(2)} \tag{A12}$$

where $\underline{\alpha}_{mn}^{(1)} = \underline{k}_{t,mn}/k_{t,mn}$ and $\underline{\alpha}_{mn}^{(2)} = \underline{z}_0 \times \underline{\alpha}_{mn}^{(1)}$. Moreover, the voltage and current waves, $v_{mn}^{(j)}$ and $i_{mn}^{(j)}$, satisfy the transmission-line equation along the z-axis, given below

$$\frac{dv_{mn}^{(j)}(z)}{dz} = ik_z Z^{(j)}i_{mn}^{(j)}(z) \tag{A13}$$

$$\frac{di_{mn}^{(1)}(z)}{dz} = ik_z Y^{(j)}v_{mn}^{(1)}(z) \tag{A14}$$

where the superscript $j = 1$ represents TE-wave and $j = 2$ for TM-wave, respectively. Notably, the wave impedances of TE- and TM- wave are

$$Z^{(1)}\left(= \frac{1}{Y^{(1)}}\right) = \frac{\omega\mu_0}{k_z} \tag{A15}$$

$$Z^{(2)}\left(= \frac{1}{Y^{(2)}}\right) = \frac{k_z}{\omega\varepsilon_0\varepsilon_s}. \tag{A16}$$

APPENDIX B
GRAPHENE TENSOR CONDUCTIVITY

By applying the Kubo formula, graphene tensor conductivity due to magnetostatic field bias is characterized using a semi-classical quantum mechanical method as follows [2], [7]:

$$
\begin{aligned}
&\sigma_d(\mu_c(E_o), B_o) \\
&= \frac{e^2 v_F^2 |eB_o| \left(\omega + i\tau^{-1}\right)\hbar}{i\pi} \\
&\times \sum_{n=0}^{\infty}\left\{
\begin{array}{l}
\frac{f_d(M_n) - f_d(M_{n+1}) + f_d(-M_{n+1}) - f_d(-M_n)}{(M_{n+1}-M_n)^2 - (\omega+i\tau^{-1})^2\hbar^2} \times \\
\left(1 - \frac{\Delta^2}{M_n M_{n+1}}\right)\frac{1}{M_{n+1}-M_n} + \\
\frac{f_d(-M_n) - f_d(-M_{n+1}) + f_d(-M_{n+1}) - f_d(M_n)}{(M_{n+1}+M_n)^2 - (\omega+i\tau^{-1})^2\hbar^2} \times \\
\left(1 + \frac{\Delta^2}{M_n M_{n+1}}\right)\frac{1}{M_{n+1}+M_n}
\end{array}
\right\}
\end{aligned} \tag{B.1}
$$

$$
\begin{aligned}
&\sigma_o(\mu_c(E_o), B_o) \\
&= -\frac{e^2 v_F^2 eB_o}{\pi} \\
&\times \sum_{n=0}^{\infty}\left\{
[f_d(M_n) - f_d(M_{n+1}) - f_d(-M_{n+1}) + f_d(-M_n)] \times \right. \\
&\left. \left[\left(1 - \frac{\Delta^2}{M_n M_{n+1}}\right)\frac{1}{(M_{n+1}-M_n)^2 - (\omega+i\tau^{-1})^2\hbar^2} + \right.\right. \\
&\left.\left. \left(1 + \frac{\Delta^2}{M_n M_{n+1}}\right)\frac{1}{(M_{n+1}+M_n)^2 - (\omega+i\tau^{-1})^2\hbar^2}\right]\right\}
\end{aligned} \tag{B.2}
$$

where

$$M_n = \sqrt{\Delta^2 + 2nv_F^2 |eB_o|\hbar}. \tag{B.3}$$

Function $f_d(\varepsilon)$ is the Fermi-Dirac distribution give below

$$f_d(\varepsilon) = \frac{1}{\exp\left(\frac{\varepsilon - \mu_c}{T}\right) + 1}. \tag{B.4}$$

Parameter ε is the energy, $-e$ is the charge of an electron, and $\hbar$ is the reduced Plank constant. Parameters μ_c is the chemical potential determined by the electrostatic bias voltage or achieved by chemical doping, T is the temperature, τ is the electron relaxation time, $v_F \approx 10^6$ m/s is the electron energy-independent velocity, and Δ is an excitonic energy gap (it is approximately equal to zero at room temperature).

REFERENCES

[1] A. K. Geim and K. S. Novoselov, "The rise of graphene," *Nature Mater.*, vol. 6, pp. 183–191, 2007.

[2] V. P. Gusynin, S. G. Sharapov, and J. P. Carbotte, "Magneto-optical conductivity in graphene," *J. Phys.: Cond. Matter*, vol. 19, p. 026222, 2007.

[3] A. Vakil and N. Engheta, "Transformation optics using graphene," *Science*, vol. 332, pp. 1291–1294, 2011.

[4] V. Ryzhii, A. Satou, and T. Otsuji, "Plasma waves in two-dimensional electron-hole system in gated graphene heterostructures," *J. Appl. Phys.*, vol. 101, p. 024509, 2007.

[5] E. H. Hwang and S. Das Sarma, "Dielectric function, screening, and plasmons in two-dimensional graphene," *Phys. Rev. B*, vol. 75, no. 20, pp. 205418–205424, 2007.

[6] G. W. Hanson, "Dyadic Green's functions and guided surface waves for a surface conductivity model of graphene," *J. Appl. Phys.*, vol. 332, pp. 064302–064308, 2008.

[7] G. W. Hanson, "Dyadic Green's functions for an anisotropic non-local model of biased graphene," *IEEE Trans. Antennas Propag.*, vol. 56, no. 3, pp. 747–757, Mar. 2008.

[8] R. Yan, B. Sensale-Rodriguez, L. Liu, D. Jena, and H. G. Xing, "A new class of electrically tuneable metamaterial terahertz modulators," *Opt. Exp.*, vol. 20, no. 27, pp. 28664–28671, 2012.

[9] R. Yan, S. Rafique, W. Li, X. Liang, D. Jena, L. Liu, B. Sensale-Rodriguez, and H. Xing, "Tuneable graphene-based metamaterial terahertz modulators," presented at the CLEO: Science and Innovation, Jun. 9–14, 2013 [Online]. Available: http://dx.doi.org/10.1364/CLEO_SI.2013.CM2J.2

[10] D. Correas-Serrano, J. S. Gómez-Díaz, and A. Alvarez-Melcon, "On the influence of spatial dispersion on the performance of graphene-based plasmonic devices," *IEEE Antennas Wireless Propag. Lett.*, vol. 13, pp. 345–348, 2014.

[11] G. Lovat, G. W. Hanson, R. Araneo, and P. Burghignoli, "Semiclassical spatially dispersive intraband conductivity tensor and quantum capacitance of graphene," *Phys. Rev. B*, p. 115429, 2013.

[12] J. S. Gómez-Díaz, J. R. Mosig, and J. Perruisseau-Carrier, "Effect of spatial dispersion on surface waves propagating along graphene sheets," *IEEE Trans. Antennas Propag.*, vol. 61, no. 7, pp. 3589–3596, Jul. 2013.

[13] G. Lovat, P. Burghignoli, and R. Araneo, "Low-frequency dominant-mode propagation in spatially dispersive graphene nanowaveguides," *IEEE Trans. Electromagn. Compat.*, vol. 55, no. 2, pp. 328–333, Apr. 2013.

[14] D. Correas-Serrano, J. S. Gómez-Díaz, J. Perruisseau-Carrier, and A. Alvarez-Melcon, "Spatially dispersive graphene single and parallel plate waveguides: Analysis and circuit model," *IEEE Trans. Microw. Theory Tech.*, vol. 61, no. 12, pp. 4333–4344, Dec. 2013.

[15] A. Fallahi and J. Perruisseau-Carrier, "Electromagnetic properties of graphene metasurfaces and applications," in *Proc. 7th Eur. Conf. Antennas Propagation*, Nov. 30, 2012, pp. 492–495.

[16] A. Fallahi and J. Perruisseau-Carrier, "Design of tuneable biperiodic graphene metasurfaces," *Phys. Rev. B*, vol. 86, pp. 195408–195417, Nov. 2012.

[17] E. Carrasco and J. Perruisseau-Carrier, "Reflectarray antenna at Terahertz using graphene," *IEEE Antennas Wireless Propag. Lett.*, vol. 12, pp. 253–256, 2013.

[18] O. V. Shapoval, J. S. Gomez-Diaz, J. Perruisseau-Carrier, J. R. Mosig, and A. I. Nosich, "Integral equation analysis of plane wave scattering by coplanar graphene-strip gratings in the THz range," *IEEE Trans. Terahertz Sci. Technol.*, vol. 3, no. 5, pp. 666–674, Sep. 2013.

[19] R. Mittra, C. H. Chan, and T. Cwik, "Techniques for analyzing frequency selective surfaces-A review," *Proc. IEEE*, vol. 76, no. 12, pp. 1593–1615, Dec. 1988.

[20] M. G. Moharam and T. K. Gaylord, "Rigorous coupled-wave analysis of planar-grating diffraction," *J. Opt. Soc. Amer.*, vol. 71, pp. 811–818, 1981.

[21] S. T. Peng, "Rigorous formulation of scattering and guidance by dielectric grating waveguides: General case of oblique incidence," *J. Opt. Soc. Amer. A*, vol. 6, pp. 1869–1883, 1989.

[22] M. Jiang, T. Tamir, and S. Zhang, "Modal theory of diffraction by multilayered gratings containing dielectric and metallic components," *J. Opt. Soc. Amer. A*, vol. 18, pp. 807–820, Apr. 2001.

[23] L. E. R. Petersson and J.-M. Jin, "A two-dimensional time-domain finite element formulation for periodic structures," *IEEE Trans. Antennas Propag.*, vol. 53, no. 4, pp. 1480–1488, Apr. 2005.

[24] N. A. Nicorovici and R. C. McPhedran, "Lattice sums for off-axis electromagnetic scattering by gratings," *Phys. Rev. E*, vol. 50, no. 4, pp. 3143–3160, 1994.

[25] R. Petit and G. Tayeb, "Theoretical and numerical study of gratings consisting of periodic arrays of thin and lossy strips," *J. Opt. Soc. Amer. A*, vol. 7, pp. 1686–1692, 1990.

[26] A. Hessel and A. A. Oliner, "A new theory of Wood's anomalies on optical grating," *Appl. Opt.*, vol. 4, pp. 1275–1297, 1965.

[27] R. B. Hwang, "Scattering characteristics of two-dimensional periodic impedance surface," *IEEE Trans. Antennas Propag.*, vol. 48, no. 10, pp. 1521–1527, Oct. 2000.

[28] R. B. Hwang and S. T. Peng, "Guidance characteristics of two-dimensional periodic impedance surface," *IEEE Trans. Microw. Theory Tech.*, vol. 47, no. 12, pp. 2503–2511, Dec. 1999.

[29] R. C. Hall, R. Mittra, and K. M. Mitzner, "Analysis of multilayered periodic structures using generalized scattering matrix theory," *IEEE Trans. Antennas Propag.*, vol. 36, no. 4, pp. 511–517, Apr. 1988.

[30] S. T. Peng, "Rigorous analysis of guided waves in doubly periodic structures," *J. Opt. Soc. Amer. A*, vol. 6, pp. 1448–1456, 1990.

[31] R. B. (R.) Hwang, *Periodic Structures: Mode-Matching Approach and Applications in Electromagnetic Engineering*, 1st ed. Singapore: Wiley-IEEE Press, 2013.

Ruey-Bing Hwang (SM'06) received the B.S. degree from the Department of Communications Engineering, National Chiao-Tung University, Taiwan, R.O.C., in 1990, the M.S. degree from the Department of Electrical Engineering, National Taiwan University, Taiwan, R.O.C., in 1992, and the Ph.D. degree from the Institute of Electronic Engineering, National Chiao-Tung University in 1996.

From August 2004 to July 2005, he was an Assistant Professor with the Communication Engineering Department, National Chiao-Tung University, where he became a Professor with the ECE Department in August 2008. In August 2013, he was appointed Director of the Graduate Institute of Communications Engineering, which is affiliated with the ECE Department. He has authored or coauthored over 100 journal and international conference publications in the areas of microwaves, optics, and applied physics. Additionally, he authored a book entitled *Periodic Structures: Mode-Matching Approach and Applications in Electromagnetic Engineering* (Wiley-IEEE, 2013). His research interests include electromagnetic periodic structure theory, phased array technology (beam-forming and angle-of-arrival estimation), and frequency-modulated continuous-wave (FMCW) radar systems.

Dr. Hwang is currently Chair of the IEEE AP-S Taipei Chapter. He is an honor member of Phi Tau Phi.